

# Processing and interpretation of pre-flight FUSE spectra

Alexandra N. Cha, David J. Sahnou, & H. Warren Moos

Department of Physics & Astronomy, The Johns Hopkins University,  
3400 N. Charles St., Baltimore, MD 21218

## ABSTRACT

H<sub>2</sub> and Pt-Ne gas lamp spectra acquired during the pre-flight optical testing of the Far Ultraviolet Spectroscopic Explorer (FUSE) have been studied in order to refine the science data processing procedure. Using automated spectral line identification software and raytrace models of instrument point spread functions, a pre-flight optical performance assessment was completed. The method by which the raw two-dimensional FUSE detector data are converted into calibrated, one-dimensional spectra is described and illustrated using spectrograph integration and test (I & T) data. A pre-flight estimate of the resolving power of FUSE is presented along with a thorough description of the associated approximations used to convert measured values of  $\lambda/\Delta\lambda$  to resolving power. The point spread functions of data from spectrograph I & T and optical-end-to-end testing (OETE) are presented, and the test factors causing their different appearances is discussed.

## 1. PROCESSING OF FUSE SPECTRA

The Far Ultraviolet Spectroscopic Explorer (FUSE) optical design consists of four coaligned far ultraviolet channels (two have optics coated with SiC, and two with Al+LiF), each of which creates a separate spectrum on one of two double delay line detectors. Each detector, in turn, is divided into two independent segments containing  $16384 \times 1024$  pixels, resulting in eight individual spectra which must be separately processed in order to recover the ultraviolet spectrum ( $\lambda\lambda 905 - 1187 \text{ \AA}$ ) of the object being observed. Every channel contains four spectrograph apertures, HIRS ( $1.25'' \times 20''$ ), MDRS ( $4.0'' \times 20''$ ), LWRS ( $30'' \times 30''$ ), and a pinhole (diameter  $\sim 0.5''$ ). Portions of two-dimensional spectra from different telescope channels and apertures are shown in Figure 1. The shape of the spectral lines and the resolving power vary depending on the telescope channel and wavelength. The elongated lines from the LiF channel and the compact spectral lines from the SiC channel, which span different wavelength regions, are shown in Figure 1.

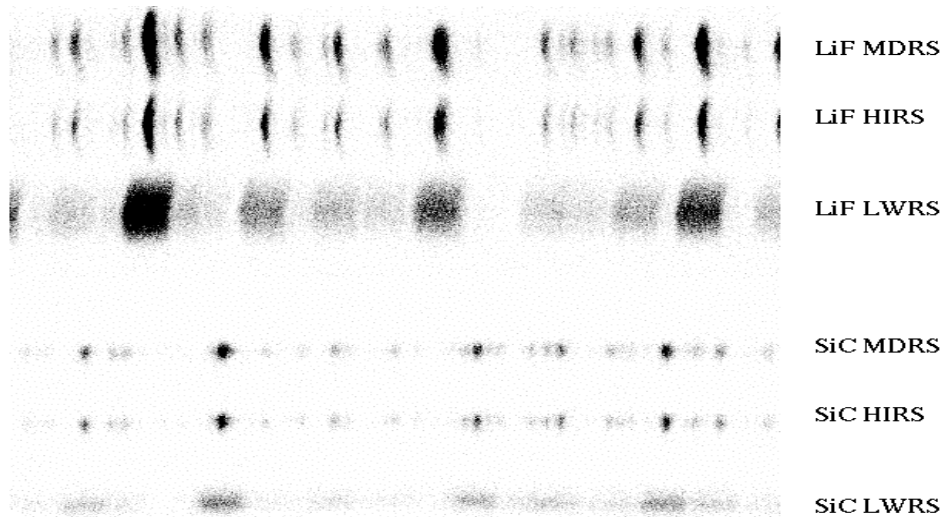


Figure 1. A portion of a FUSE detector showing the two-dimensional spectral lines imaged during spectrograph I & T, covering different wavelength regions, is depicted above. The corresponding telescope channels (LiF or SiC) and aperture names (HIRS, MDRS, and LWRS) are noted to the right of each spectrum segment. Spectra resulting from the illumination of the pinhole apertures are not shown here.

Figure 2 contains a diagram illustrating the wavelength coverage of the multiple FUSE telescope channels and detector segments. The arrangement of the detector regions in Figure 2 is not representative of the physical layout of the detector; however, it does reveal that two or more detector regions cover 94% of the bandpass, while the central 45% of FUSE's

wavelengths are imaged by three or more detector segments. The spectrograph was designed to provide this redundant wavelength coverage for two reasons. The redundancy is valuable in that if one channel fails, the data for the associated bandpass is likely to have been secured on another. Conversely, if all channels operate nominally, duplicate spectra from different channels provide data at various resolving powers that could be combined to increase the signal-to-noise ratio.

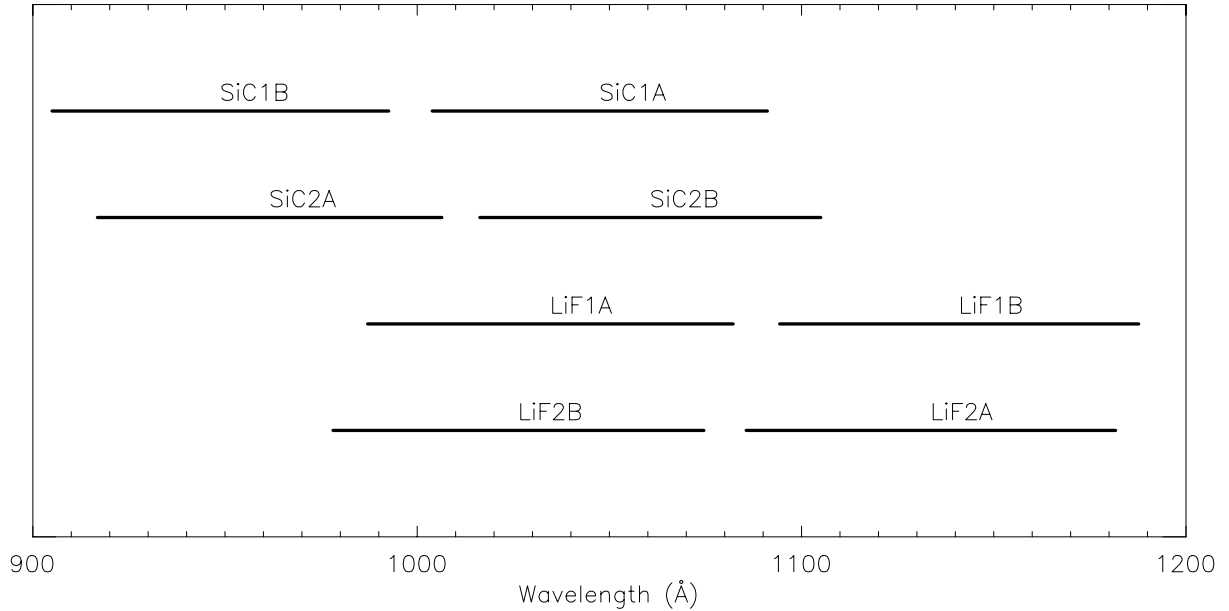


Figure 2. Wavelength coverage of FUSE's eight detector regions is shown. A LiF region is in the top panel and a SiC region is shown in the bottom panel. Note that SiC1A and LiF1A are on the same physical segment, as are SiC1B & LiF1B, SiC2A & LiF2A, and SiC2B & LiF2B.

### 1. From Raw Data to Science Spectra

With each observation, FUSE produces eight two-dimensional spectra—two from each of its four apertures. In most cases, very little flux is incident on the smallest aperture (~0.5 arcsec diameter pinhole) and no spectra were processed for the pinhole aperture. Note that although the data are two dimensional, little or no spatial information about the target is available at most wavelengths since the two dimensional point spread functions are simply a byproduct of the optical design<sup>1</sup>. The information in a two-dimensional FUSE spectrum is equivalent to the information in a one-dimensional flux versus wavelength spectrum; therefore the FUSE data are transformed in the data processing pipeline to the simpler one-dimensional form. In this section, the process and methodology used to extract and calibrate these one-dimensional flux versus wavelength science spectra are described.

The first step in the data processing involves correcting the astigmatism due to the optical design. The astigmatism causes the two-dimensional images of the spectral lines to vary with wavelength. A detailed description of the aberrations associated with FUSE's holographically ruled grating may be found in Chambord *et al.* (1996)<sup>2</sup>. The results of the astigmatism appear as line curvature, as seen in the portions of H<sub>2</sub> spectra shown in Figures 1 and 3.

Figure 3 contains a portion of a spectrum from a LiF channel (top) and one from a SiC channel (bottom) covering approximately the same wavelength range. Since the dispersion is different for the two channels, the spectral lines are not perfectly aligned. In addition, for ease of comparison, the SiC spectrum has been reflected about the y-axis and then plotted so that wavelength increases in the same direction as the LiF spectrum. The description of the main science data processing steps will be illustrated by pictorially following the progress of these two segments in Figures 3-7.

If the two dimensional spectrum in Figure 3 were to be collapsed along the line-height axis at this point, the resulting one-dimensional spectrum would contain artificially broadened lines due to the line curvature. Straightening the spectral lines first allows much of the astigmatism to be corrected and resolving power to be increased. Again recall that although the spectra output by FUSE are two dimensional, they contain no spatial resolution, so such manipulation of the two-dimensional spectra does not cause a loss of data content.

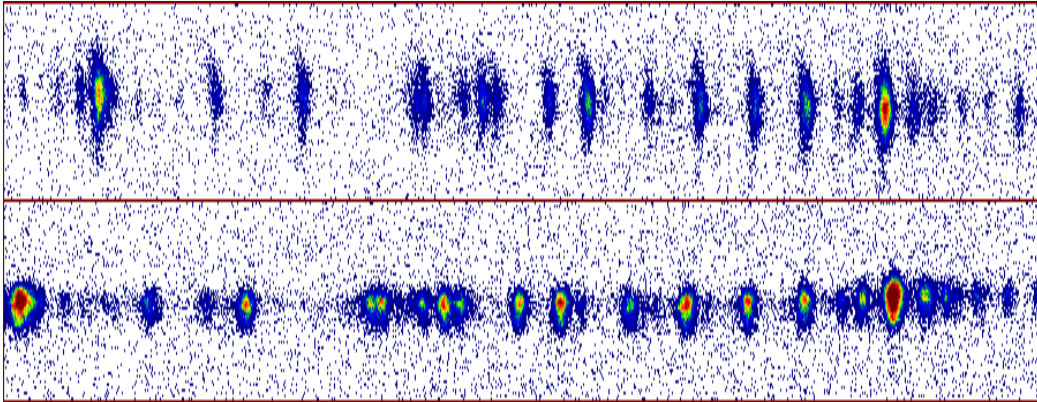


Figure 3. Regions from unprocessed two-dimensional FUSE spectra. The upper panel is from a LiF channel and the lower panel is from a SiC channel reflected about the y-axis. These two segments cover approximately the same wavelength range,  $\lambda\lambda 1089\text{-}1095 \text{ \AA}$ , but have slightly different dispersions.

To straighten the spectral lines, an algorithm was developed whereby a 2<sup>nd</sup> degree polynomial is fit along the length of each line. Next, the pixel with the greatest intensity from each row of pixels immediately surrounding the spectral line was identified. These pixels containing the peak intensities, along with the surrounding pixels, were shifted so that the peak intensity pixels were aligned vertically with the vertex of the parabolic fit. Other methods of straightening the line were explored, but the alternate methods neither improved the resulting spectral resolving power, nor implied that the parabola fitting method introduced errors in the spectrum associated with misidentification of lines after wavelength calibration. Figure 4 depicts the same spectra shown in Figure 3 after line straightening. It is clear from the spectral segments presented that here, the LiF channel's lines are narrower than the SiC channel's lines, i.e. the LiF channel here has higher resolving power than the SiC channel—a consequence of the optical design. Line straightening thus improves the resolving power for the LiF segment's spectrum since the extent of the curvature is greater than the width of the line. In the actual pipeline, each line will not be individually corrected in the manner described here, but model point spread functions that vary with wavelength will be used to correct for the astigmatism.

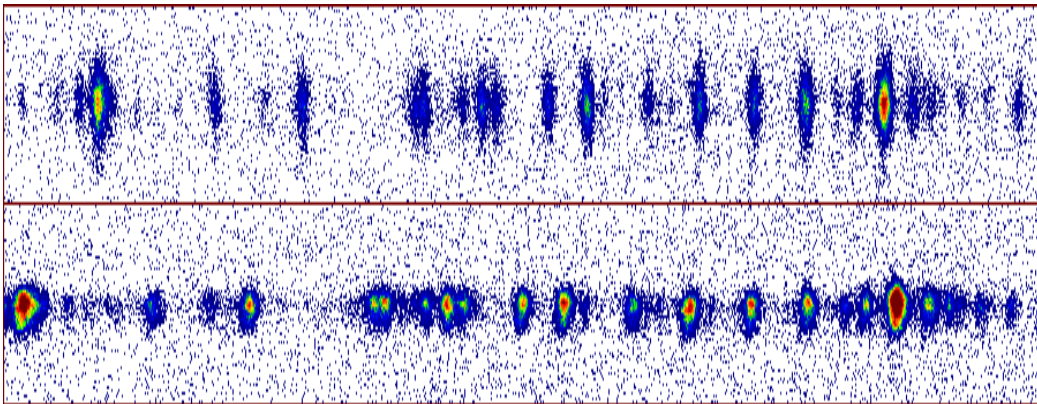


Figure 4. Two segments of astigmatism corrected, two-dimensional FUSE spectra. A LiF region is shown in the top panel and a SiC region is in the bottom panel. These segments cover the approximate wavelength range,  $\lambda\lambda 1089\text{-}1095 \text{ \AA}$ , as in Figure 3.

The second science data processing step is the extraction of one-dimensional spectra from the two-dimensional astigmatism-corrected spectra. To improve the signal-to-noise ratio of the one-dimensional spectra, only a portion (the extent is wavelength and channel dependent) of each two-dimensional spectrum is extracted, with the center portion weighted more heavily than the edges. The spectra are next summed over the reduced y-range, producing a vector ( $1 \times 16384$ ) containing counts as a function of x-pixel. The spectra from the two detector segments shown in the previous figure been extracted and collapsed to one-dimension as seen in Figure 5. Notice that the segments contain the same spectral lines, but since the pixel-to-wavelength conversion is non-linear, the lines are spaced slightly disparately. The different pixel labels simply reflect that each detector region has a unique bandpass, and therefore, a given wavelength appears at a different pixel number on each channel.

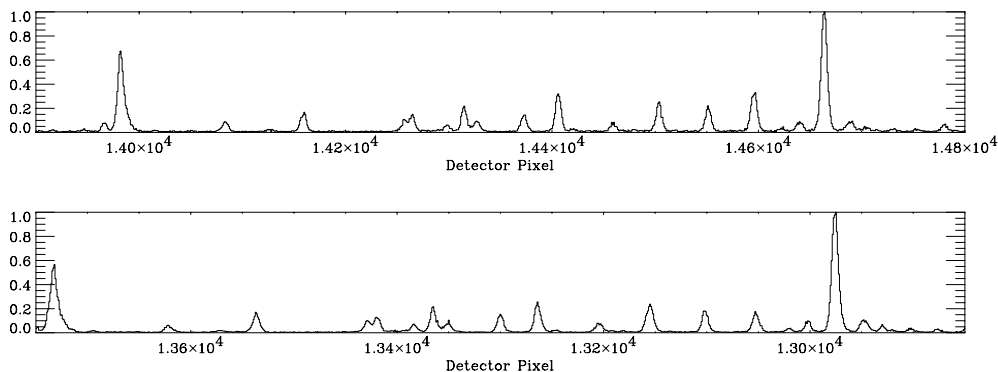


Figure 5. The extracted FUSE spectral segments from Figure 4 are shown here after having been collapsed to one-dimension. A LiF region is shown in the top panel and a SiC region is in the bottom panel. Note that the line heights have been arbitrarily normalized.

The third step towards attaining useable science spectra is determining a wavelength calibration. Useful science spectra must contain counts as a function of wavelength, so the wavelength calibration will be the solution that allows pixels to be converted to wavelengths.  $H_2$  gas lamp emission line spectra were observed during the integration and testing (I & T) of the spectrograph, and have been used in conjunction with data from a high-resolution atlas of ultraviolet  $H_2$  emission lines<sup>3</sup>. A template spectrum has been created by convolving the  $H_2$  atlas data, which includes the intensity and wavelength of observed emission lines, with a Gaussian line shape having approximately the same FWHM as the spectra obtained during FUSE I & T. The template and data spectra were cross-correlated to match up the centroids of the data and template emission lines obtaining approximately 100 pixel locations with corresponding wavelengths on each detector region. Approximately half of the LiF detector region shown in Figure 5 is repeated in Figure 6.

Figure 6. Half of the spectrum of the LiF detector region shown in Figure 5 (see corresponding pixel numbers) with the FUSE data spectrum in black and the template spectrum created with the  $H_2$  atlas data overplotted in gray.

In addition, the corresponding portion of the template spectrum created from the H<sub>2</sub> atlas data is overplotted in gray. The emission lines from the data spectrum (black) on the right end of the figure are slightly offset from the template emission lines, illustrating the non-linear relationship between pixels and wavelength due to the FUSE detectors. The final pre-flight dispersion solution was determined by fitting a high order Chebyshev polynomial to pixel-wavelength pairs obtained during the cross-correlation of the template and data spectra. Additional in orbit calibrations will be necessary to correct for launch shifts, the slight component shifts due to 1-G gravitational release, and temperature fluctuations. Figure 7 presents wavelength calibrated one-dimensional spectra for the detector segments previously presented. Note that with one observation, two spectra with overlapping wavelength coverage, but different resolving powers were obtained.

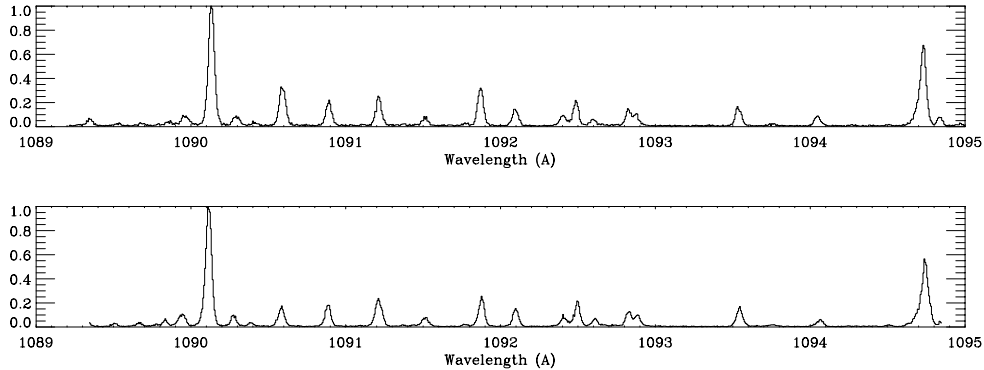


Figure 7. Segments of wavelength calibrated FUSE spectra are shown. A LiF region is in the top panel and a SiC region is shown in the bottom panel. Again, the line heights have been arbitrarily normalized.

In practice, more procedures than have been described are required to transform raw data to science data. Outlined below are all of the processing phases included in the actual science data processing pipeline<sup>4</sup>.

1. Data Screening — Bad data is flagged and excluded from further processing.
2. Doppler Shift Calculation — Determination of the Doppler shift correction that must be applied to each photon, given that the motion of the satellite and the arrival time of each photon are known.
3. Binning to an Image — Creation of a full detector sized, two-dimensional spectral image of the segment.
4. Drift Correction — A shift and stretch of the detector's analog electronics scale occurs as temperature changes, so these effects are modeled and then used to correct the data.
5. Background Subtraction — Detector's background count rate, typically  $< 1 \text{ count s}^{-1} \text{ cm}^{-2}$  on the ground, is subtracted from the spectra.
6. Flat Field Correction — On board stimulation lamps after launch, and deep flat fields obtained before launch, are used to obtain exposures revealing detector features that are divided out from the spectra.
7. Geometric Distortion Correction — Nonlinearities in the x- and y-directions of the detector are modeled and their distortion effects on the spectra are removed.
8. Astigmatism Correction — Two-dimensional spectral lines are straightened to remove effects of astigmatism induced by the optical design (as described above).
9. Spectral Extraction — A two-dimensional region containing the spectral lines is extracted and summed over y-pixels to create a one-dimensional spectrum (as described above).
10. Wavelength Calibration — Data from I & T or on orbit is used to apply a dispersion solution, whereby each pixel is assigned a wavelength (as described above).
11. Dead Time Correction — For photometrically calibrated data, the difference between the number of events stored by the flight computer and the number of photons actually reaching the detector must be known, and an appropriate correction factor must be applied to the data.
12. Flux Calibration — A flux versus count rate calibration will be determined for each channel in orbit from a white dwarf observation program.
13. Combining Spectra — The eight independent spectra will be resampled and combined creating a single flux versus wavelength spectrum with increased signal-to-noise.

## 2. INTERPRETATION OF PRE-FLIGHT SPECTRA

Spectral data has been obtained during two phases of the development of the FUSE mission, first during spectrograph I & T at the University of Colorado, and second during optical end-to-end (OETE) testing at NASA's Goddard Space Flight Center. In the first instance, the testing involved the spectrograph only, and the slits were fully illuminated with windowless lamps ( $H_2$  or Pt-Ne) providing light across the entire FUSE bandpass<sup>5</sup>. By the time of OETE, the entire instrument (spectrograph + telescope mirrors) had been assembled. Lamps with LiF coated windows, which reduced the effective bandpass, were used with external collimators to illuminate the primary mirrors. For a detailed description of the operational set-up and test see Conard *et al.* (1999)<sup>6</sup>. In this portion of the paper, a comparison of the illumination and resulting spectral line shapes, the methods used to focus, and the data acquired to predict the resolving power of FUSE in the two tests is provided.

### 1. Illumination & Line Shapes

During I & T, the slits were almost fully illuminated and the entire bandpass of the spectrograph received incident photons. These two factors contributed to the imaging of a complete spot on the detector—one closely resembling spots imaged by a "virtual FUSE," created using raytrace software. OETE, on the other hand, presented the challenges of under-illuminated mirrors and a reduced bandpass of  $\sim 1050 - 1187 \text{ \AA}$ , due to the LiF windows on the lamps. These constraints resulted in the imaging of partial spectral lines. To illustrate, Figure 8 shows two enlarged two-dimensional spectral lines, the one on the left was obtained during spectrograph I & T and the one on the right was obtained during OETE.

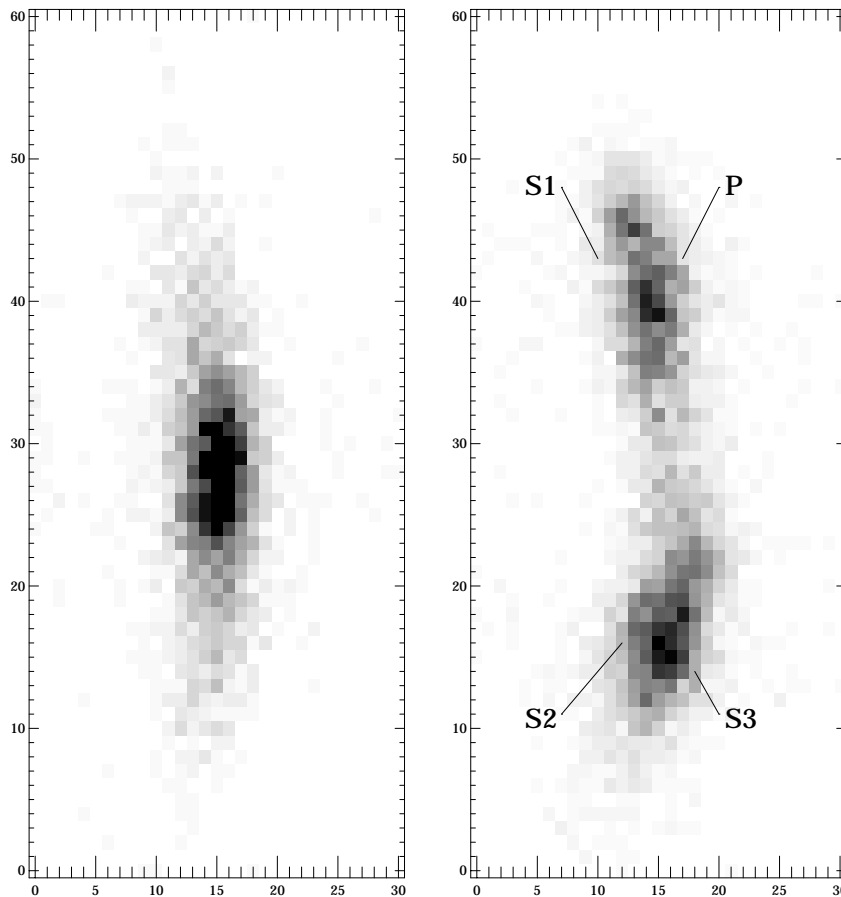


Figure 8. A pair of two-dimensional Pt-Ne  $\lambda 1152.58 \text{ \AA}$  lines. The spectral line on the left was obtained during I & T, while the spectral line on the right is a composite of four exposures, each illuminated with a different source during OETE. The portion of the spectral line imaged by each lamp (S1, S2, S3, P) has been labeled on the diagram. The combination of the four apertures during OETE does not illuminate the full mirror creating the incomplete spectral line on the right. The gray-scaling of the images is not the same. The I & T line, with its flux concentrated in the center, is much brighter than the OETE line. The darker top and bottom ends in the OETE line would appear as a light gray in the gray-scale of the I & T line, but we have enhanced the scaling to show the structure.

The lines shown are from the same detector segment, LiF2A, and are actually the same Pt-Ne spectral line at the wavelength 1152.58 Å. The I & T line has most of the intensity located at the center of the line, as is expected, whereas the OETE line has a double peaked concentration of intensity above and below the center of the line. The different portions of the spectral line have been produced by light from the four lamps used to (partially) illuminate the primary mirror during four separate exposures in OETE testing. The absence of signal at the center of the OETE line in Figure 8 arises because the center of the primary mirror during OETE was not illuminated. Three apertures, S1, S2, and S3 were identical slits with dimension 15µm × 55µm, representing stars. The fourth aperture, P, was circular with a diameter of 150µm, and was to represent light from an extended source, such as a planet. The lamps illuminating the four apertures were identical. In Figure 8, the regions of the OETE spectral line have been labeled with the name of the aperture from whose light they were imaged.

## 2. Focusing Method & Status

The distinct testing conditions of spectrograph I & T and OETE and the dissimilar spectral data obtained during the two required that different methods of determining best focus be developed. In addition to the contrasting illumination conditions described in section 2.1, H<sub>2</sub> lamp spectra were primarily used during spectrograph I & T for two reasons. First, the high resolution H<sub>2</sub> atlas<sup>3</sup> could be used to compare to the FUSE data spectra for calibration purposes. Second, the spectrum of H<sub>2</sub> is very rich in the FUSE bandpass, so there are many spectral lines having medium to high intensities, whereas Pt-Ne lines are sparse in comparison (~ 50% fewer lines per Angstrom).

The monochromatic spots that comprised the two-dimensional spectral lines from spectrograph I & T tended to narrow (in the direction of the dispersion axis) as the spectrograph approached focus and broaden as the system moved out of focus. Since the entire bandpass was covered, many H<sub>2</sub> lines (approximately 100 for the H<sub>2</sub> lamp) could be identified in each of the detector regions, and a statistically significant average FWHM could be calculated. By locating the focal position of the minimum average FWHM, which corresponds to the maximum average  $\lambda/\Delta\lambda$ , the spectrograph's "best focus" position was determined. The focal plane assemblies and the gratings were movable during spectrograph I & T to enable focusing. Figure 9 illustrates the effect that focal position has on the measured  $\lambda/\Delta\lambda$ . Spectra were obtained at five successive locations of the focal plane assembly passing through best focus at position 3—where the narrowest spectral lines were obtained.

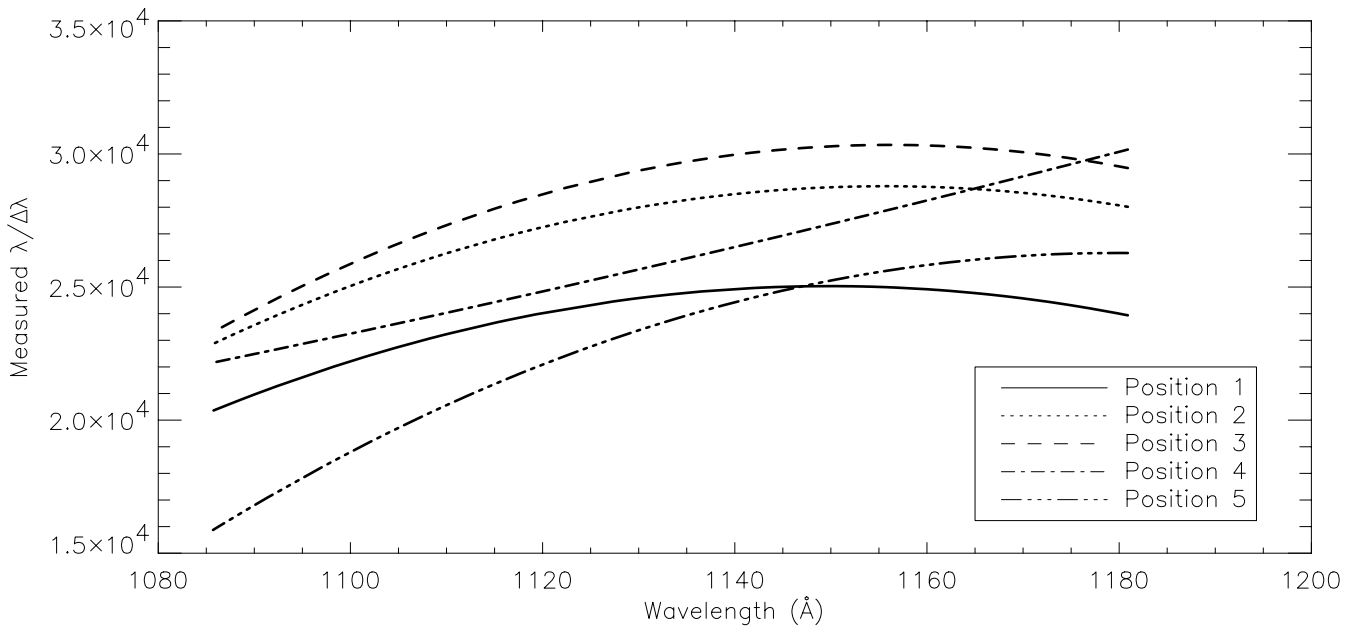


Figure 9. Polynomial fit to the measured values of  $\lambda/\Delta\lambda$  on a LiF2A detector region using H<sub>2</sub> spectra obtained during I & T at five successive focal positions. Position 3 produces the highest  $\lambda/\Delta\lambda$ , so the best focus position is nearest this spectrograph configuration.

At OETE, the gratings had been locked into their final positions and could not be moved and the focal plane assemblies were limited to their smaller flight range. The instrument and spacecraft had been mated, and the purpose of the OETE testing was to verify that no major problems existed with the instrument performance. Pt-Ne lamps were used to

illuminate the telescope, perform coarse focus runs, and check that spectral lines were imaging correctly and were comparable to the results of spectrograph testing during I & T.

To obtain measurements that would check the quality of the output spectral lines, the instrument was first focused. A different method for determining the focus utilizing the partial spectral lines (see Figure 8) was developed for OETE. The physical motivation behind the new focusing method was based upon the fact that when the instrument was out of focus, light of a particular wavelength incident on various parts of the primary mirror did not get imaged to a tight spectral line, but was imaged to slightly different locations. When the instrument was in focus, however, monochromatic light which had been reflected off different sections of the mirror was imaged to narrow (curved—due to the astigmatism) spectral lines. Using this basic premise of geometrical optics, the position of best focus was measured when the centroids of the two spots created by lamps S2 and S3 (see Figure 8) overlapped.

At the conclusion of the OETE testing, the position of best focus had been attained, but the instrument was not launched in-focus, since the physical conditions in orbit are different. Models predicting the motion of structures within the instrument after launch include three chief factors: 1-G gravitational release, moisture desorption, and on-orbit thermal conditions<sup>7</sup>. The loss of gravity and the new thermal environment are conditions that remain constant; however, at the beginning of the mission, the instrument structure contains moisture that will begin to outgas, slowly varying the positions of optical elements and shifting the focus from that at the beginning of life. The adjustable focal plane assembly will compensate for motions due to moisture desorption on orbit. Prior to launch, the spectrograph was aligned and focused to account for these variables, so that after launch, the FUSE instrument would be close to focus.

### 3. Measurements of Resolving Power

Determining the resolving power of the spectrograph was one of the essential indicators used to conclude that the FUSE optical system was in focus and performing properly. The resolving power of the instrument impacts and determines the scientific programs that may be pursued with FUSE. A brief overview of the estimated resolving power is given by Friedman *et al.*<sup>8</sup>, whereas here a description how the resolving power was estimated is presented, and several subtleties associated with the underlying measurements are discussed. The estimated resolving power (see below) of all eight detector regions is displayed in Figure 10. The styles of the lines indicate which channel (SiC or LiF) and which side (1 or 2) of the detector is characterized. The segment, A or B, is shown by the use of a black or a gray line, respectively.

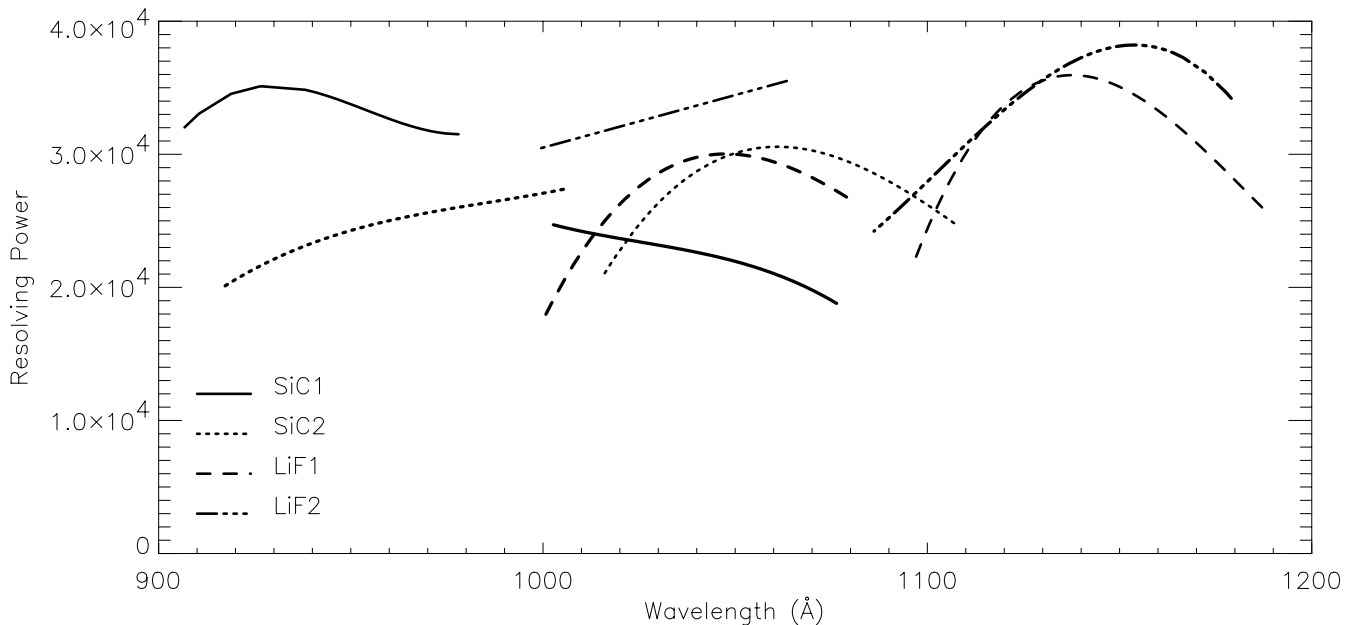


Figure 10. The estimated in-flight resolving power of the detector regions of FUSE based on pre-launch measurements. The channels (SiC or LiF) and the sides (1 or 2) of the detector are depicted by various line styles as indicated on the plot, while the segment classification, A or B, is revealed by a black or gray line, respectively. The estimated resolving power shown here includes a 15% increase over the measured values of  $\lambda/\Delta\lambda$  as described in the text.

Resolving power is defined as  $R = \lambda/\Delta\lambda$ , where  $\lambda$  is wavelength and  $\Delta\lambda$  measures the width of a spectral line at a given wavelength for a stellar point source with a line of negligible spectral width. Specifically,  $\Delta\lambda$  is the product of the FWHM of a spectral line (in pixels), the pixel size in the direction of dispersion (for FUSE:  $\sim 6 \mu\text{m}/\text{pixel}$ ), and the dispersion. The dispersion varies depending on the detector region; these values are presented in Table 1.

Table 1.

<b>Detector Region</b>	<b>Avg. Dispersion (<math>\text{\AA}/\text{mm}</math>)</b>
SiC1A & SiC1B	1.03
SiC2A & SiC2B	1.03
LiF1A & LiF1B	1.11
LiF2A & LiF2B	1.12

During spectrograph I & T and OETE, long exposures were executed to obtain high signal-to-noise spectra. To determine the resolving power of a region, detector data files were converted to one-dimensional science spectra and the FWHM of select lines was measured. The spectral lines included in the resolving power assessment were somewhat narrow (FWHM < 15 pixels) and had at least moderate signal-to-noise ratios (S/N > 10). The individual FWHM measurements were converted to values of  $\lambda/\Delta\lambda$ , and a low order polynomial (1<sup>st</sup>-3<sup>rd</sup>) was fit to the data points to obtain a conservative measure of  $\lambda/\Delta\lambda$  for each detector region. Figure 11 illustrates the measured  $\lambda/\Delta\lambda$  of the individual spectral lines (crosses) from a LiF1A H<sub>2</sub> spectrum and the corresponding cubic least squares fit. The plethora of H<sub>2</sub> lines, some of which are still unresolved blends at FUSE's resolving power, contributes to the spread in the values of  $\lambda/\Delta\lambda$  over small wavelength ranges. Conceivably, the measured  $\lambda/\Delta\lambda$  could have been defined by an upper envelope fit to the data points since FUSE was resolving spectral lines at this level. However, to ensure a conservative measurement of  $\lambda/\Delta\lambda$ , the polynomial fit was employed throughout the analysis.

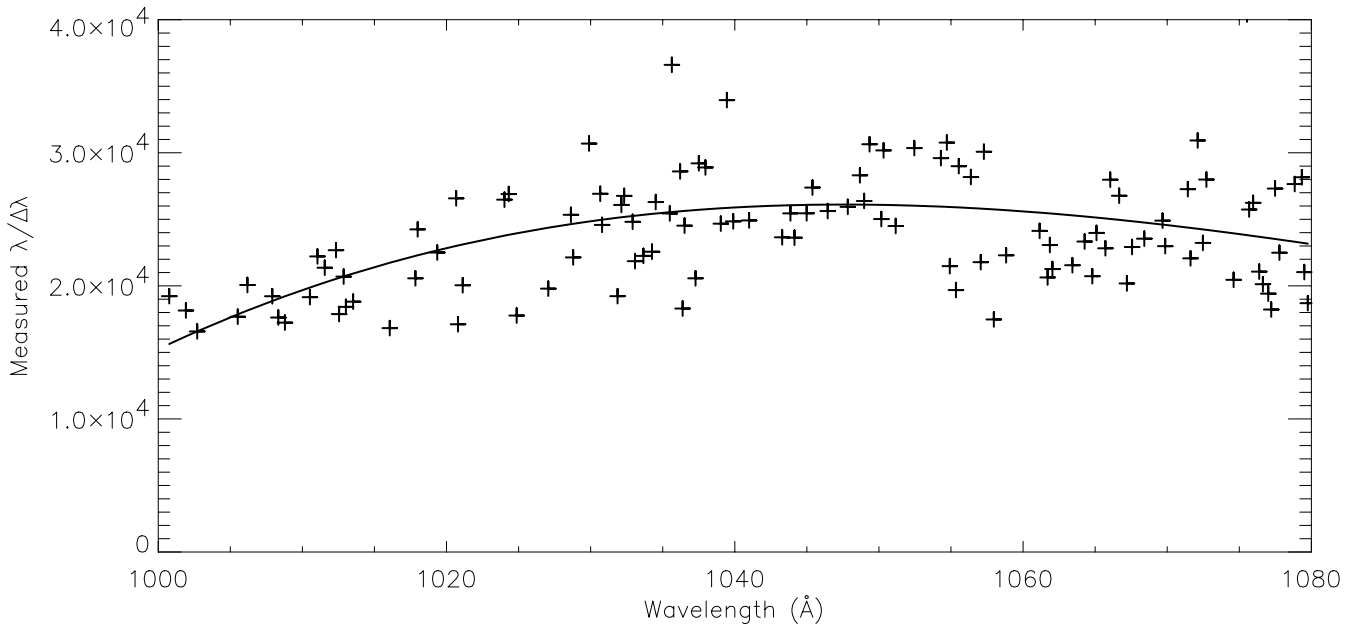


Figure 11. Measured  $\lambda/\Delta\lambda$  of an H<sub>2</sub> spectrum obtained during I & T on LiF1A. The curve is a cubic polynomial least squares fit to the data. The curve fit to the data shown here is the same as that for LiF1A in Figure 10 except it does not include the estimated 15% increase to account for degradation of the resolving power caused by testing conditions.

The LiF1A data in Figures 10 and 11 has been extracted from the same spectrum. Notice, however, that the LiF1A curve in Figure 10, the estimated resolving power plot, is slightly higher than in the measured values of  $\lambda/\Delta\lambda$  of Figure 11. Before discussing the conversion from measured  $\lambda/\Delta\lambda$  to estimated resolving power, note two crucial points: (1) as discussed below, the measured values of  $\lambda/\Delta\lambda$  are expected to be below the true resolving power and hence a correction is necessary to

obtain the correct values. (2) A conservative analysis of the data may have also biased the measured values lower. No correction has been made for the second effect.

Three factors contribute to lowering the measured values of  $\lambda/\Delta\lambda$ . These issues must be identified before estimating the on-orbit resolving power of FUSE. First, in spectrograph I & T, where the best characterization of  $\lambda/\Delta\lambda$  was made, the optics were not illuminated by a point source. The test image filled the spectrograph aperture and there were asymmetries in the grating illumination—both conditions which decreased the measured values of  $\lambda/\Delta\lambda$ . Based on a raytrace analysis, a  $\sim 5\%$  increase in  $\lambda/\Delta\lambda$  has been adopted to account for the difference between the illumination conditions present during testing and the point source illumination criterion specified in the definition of resolving power.

The second and third issues that increase the difference between measured and estimated resolving power pertain to the blending of the  $H_2$  lines and to potential intrinsic broadening of individual lines. It is difficult to distinguish between the two, but it appears that both effects exist. As mentioned earlier, the  $H_2$  spectra contain many lines that appear to be blended together at the resolving power of FUSE. During the data processing stage, lines with FWHM greater than  $\sim$ twice the expected FWHM were eliminated from the data set. Lines that pass this criterion are not all single resolved lines; unfortunately many blends are accepted too. The limiting FWHM could not be reduced further else an artificially high resolving power might be calculated in conjunction with a reduction in sampling over the bandpass.

The other spectral characteristic that increases the measured FWHMs is the difference in the intrinsic line width of  $H_2$  versus Pt-Ne. After comparing  $H_2$  and Pt-Ne spectra obtained under the same conditions during spectrograph I & T, the  $H_2$  lines appear distinctly broader than the Pt-Ne lines. To illustrate, the measured  $\lambda/\Delta\lambda$  of LiF1B with an  $H_2$  spectrum (solid line) and a Pt-Ne spectrum (dotted line) has been plotted in Figure 12. For LiF1B, the measured  $\lambda/\Delta\lambda$  is  $\sim 10\%$  higher according to the Pt-Ne data as opposed to the  $H_2$  data. Examination of the spectrograph I & T data set shows that overall the measured  $\lambda/\Delta\lambda$  is  $\sim 7 - 13\%$  higher when Pt-Ne spectra are used instead of  $H_2$  spectra. The magnitude of the effect is larger for segments with inherently better resolving power. As a result, an additional  $\sim 10\%$  increase in  $\lambda/\Delta\lambda$  due to a combination of line blending and  $H_2$  intrinsic line width is also applied to the measured values of  $\lambda/\Delta\lambda$  and is incorporated into the data in the estimated resolving power plot (Figure 10).

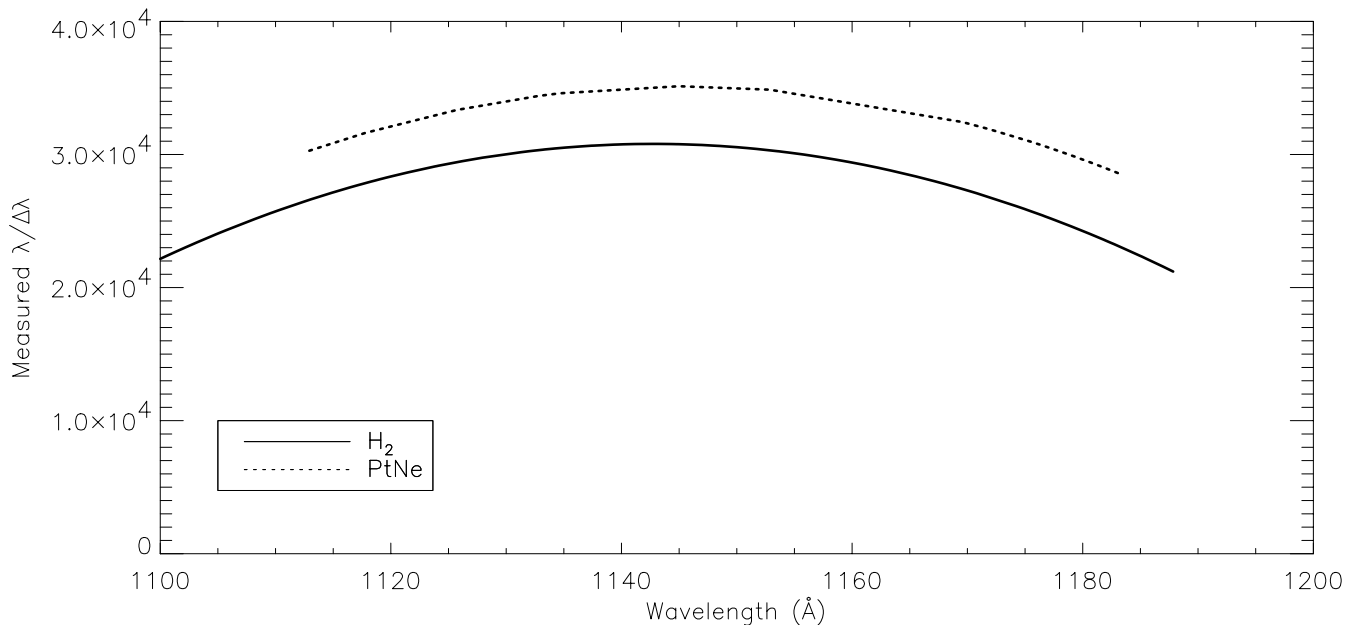


Figure 12. The 2<sup>nd</sup> order polynomial fits to the measured  $\lambda/\Delta\lambda$  of LiF1B using an I & T  $H_2$  spectrum (solid line) and an I & T Pt-Ne spectrum (dotted line).

### 3. CONCLUSIONS

In preparation for the launch and deployment of FUSE, we have developed an algorithm to process FUSE spectral data, portions of which have been modified for the actual FUSE science data pipeline. A pre-flight wavelength calibration has been established primarily based upon H<sub>2</sub> lamp spectra obtained by the FUSE spectrograph and an atlas of the ultraviolet H<sub>2</sub> spectrum. This calibration data will be iterated upon and modified during flight by using data collected in orbit. Spectrograph I & T data demonstrate that the instrument is capable of attaining resolving powers above specified requirements. Spectral data from the OETE tests performed on the integrated satellite confirm that the instrument operates as expected when compared to the more detailed spectrograph I & T data sets, and establishes that, as launched, the spectrograph can be focused on orbit.

### REFERENCES

1. Green, J.C., Wilkinson, E., & Friedman, S.D., "Design of the Far Ultraviolet Spectroscopic Explorer spectrograph," *Proc. SPIE* **2283**, pp. 12-19, 1994.
  2. Chambord, S., Grange, R., Flamand, J., Saisse, M., & Reynaud, J.-L., "Holographic gratings for the far ultraviolet: efficiency tests of two prototypes," *ApOpt* **35**, p. 3653, 1996.
  3. Roncin, J.-Y. & Launay, F., *Atlas of the Vacuum Ultraviolet Emission Spectrum of Molecular Hydrogen*, Journal of Physical and Chemical Reference Data, Monograph no. 4, American Institute of Physics, New York, 1994.
  4. Sahnou, D.J. *et al.*, "Processing of Spectra for the Far Ultraviolet Spectroscopic Explorer (FUSE)," *BAAS* **193**, 1211, 1999.
  5. Wilkinson, E., Green, J.C., Osterman, S.N., Brownsberger, K.R., & Sahnou, D.J., "Integration, alignment, and initial performance results of the Far Ultraviolet Spectroscopic Explorer (FUSE) spectrograph," *Proc. SPIE* **3356**, pp. 18-29, 1998.
  6. Conard, S.J. *et al.*, "Hardware and methods of the optical end-to-end test of the Far Ultraviolet Spectroscopic Explorer (FUSE)," *Proc. SPIE* **3765**, (this volume), 1999.
  7. Sahnou, D.J., VanDyke, C.M., Gong, Q., Bremer, J., & Kennedy, M.J., "Optical performance budget for the Far Ultraviolet Spectroscopic Explorer," *Proc. SPIE* **2863**, pp. 27-35, 1996.
  8. Friedman, S.D. *et al.*, "Pre-launch optical tests and performance estimates of the Far Ultraviolet Spectroscopic Explorer satellite," *Proc. SPIE* **3765**, (this volume), 1999.
-